

# Advanced YOLO-Based Real-Time Power Line Detection for Vegetation Management

Shuaiyang Rong , Lina He , Salih Furkan Atici , and Ahmet Enis Cetin , *Fellow, IEEE*

**Abstract**—Power line infrastructure is a key component of the power system, and it is rapidly expanding to meet growing energy demands. Vegetation encroachment is a significant threat to the safe operation of power lines, requiring reliable and timely management to enhance the resilience and reliability of the power network. Integrating smart grid technology, especially aerial drones (AD), provides substantial potential to revolutionize the management of extensive power line networks with advanced imaging techniques. However, processing the vast quantity of images captured by AD patrols remains a significant challenge. This paper introduces an intelligent real-time monitoring framework for detecting power lines and adjacent vegetation. It is developed based on the deep-learning Convolutional Neural Network (CNN), You Only Look Once (YOLO), renowned for its high-speed object detection capabilities. Unlike existing deep learning-based methods, this framework enhances accuracy by integrating YOLOv8 with directional filters. They can extract directional features and textures of power lines and their vicinity, generating Oriented Bounding Boxes (OBB) for more precise localization. Additionally, a post-processing algorithm is developed to create a vegetation encroachment metric for power lines, allowing for a quantitative assessment of the surrounding vegetation distribution. The effectiveness of the proposed framework is demonstrated using a widely used power line dataset.

**Index Terms**—Power line detection, monitoring, CNN, YOLOv8, vegetation management, AD.

## I. INTRODUCTION

POWER lines can produce sparks upon tree contact due to factors such as line sag, tree growth, and severe weather conditions during natural hazards. Tree-contacted power line sparking has been identified as a significant cause of the most destructive wildfires in California in recent years [1], as well as the devastating Maui fire in 2023 [2]. The American power grid has more than 500,000 miles of high-voltage transmission lines and 5 million miles of distribution lines, and it is still rapidly growing with decarbonization initiatives [3]. Inspecting such a large infrastructure is both labor-intensive and time-consuming, relying on traditional methods like manual patrols and helicopter

Received 31 January 2025; revised 9 May 2025; accepted 17 May 2025. Date of publication 9 June 2025; date of current version 25 July 2025. This work was supported by USDA Forest Service 24-CR-11261925-057. Paper no. TPWRD-00142-2025. (*Corresponding author: Ahmet Enis Cetin.*)

Shuaiyang Rong, Lina He, and Ahmet Enis Cetin are with the Electrical and Computer Engineering Department, University of Illinois Chicago, Chicago, IL 60607 USA (e-mail: srong4@uic.edu; lhe@uic.edu; aeccy@uic.edu).

Salih Furkan Atici is with Universitat zu Lübeck, Institut für Medizinische Informatik, Ratzeburger Allee 160, 23562 Lübeck Schleswig-Holstein, Germany (e-mail: satici2@uic.edu).

Color versions of one or more figures in this article are available at <https://doi.org/10.1109/TPWRD.2025.3578274>.

Digital Object Identifier 10.1109/TPWRD.2025.3578274

surveys that have been in use for decades. Ground patrols allow thorough evaluations but are slow and costly, while helicopter surveys cover more areas quickly but with lower detection accuracy. Both approaches rely heavily on human visual observation, increasing the risk of missed or incorrect assessments [4].

### A. Vegetation Monitoring for Power Line Inspections

Satellite imagery has been studied for vegetation monitoring within power line corridors. Sensors like Synthetic Aperture Radars (SAR) [5], operating in the microwave region of the electromagnetic spectrum, and optical sensors [6], capturing multispectral data in the visible and near-infrared regions, have been widely explored. Some studies [7], [8], [9] have used multispectral stereo pairs of satellite images to identify trees with extracted Normalized Difference Vegetation Index (NDVI) information to evaluate encroachment to power lines; however, capturing stereo images is technically challenging and costly for large-scale monitoring [10]. Recent studies focused on monocular satellite imagery combined with a machine learning technique, i.e., Adaboost classifier [11] and Support Vector Machine (SVM) [12] for extracting, segmenting, and classifying trees. However, these methods are constrained by data availability in low-light or cloudy conditions. Additionally, in these studies, the positions of power lines are typically predetermined, as they struggle to automatically detect power line conductors and bundles. Even the highest-resolution imagery is often too coarse to capture the thin and small features of power lines, particularly distribution lines, which are smaller, positioned lower, and frequently obscured by trees, making them unsuitable for fine-scale detection.

Fixed vision sensors [13] and ground-based vehicles [14] have been explored for higher-resolution data acquisition, but their limited view angles present challenges. In contrast, airborne Light Detection and Ranging (LiDAR) three-dimensional (3D) modeling with higher flexibility, has gained greater attention in the industry, typically employing fixed-wing aircraft or helicopters. Utilities such as Pacific Gas and Electric (PG&E) and Duke Energy have utilized LiDAR to assess risks near power lines [15], [16]. Existing studies [17], [18], [19], [20] showed that power line clustering, as well as the extraction and classification of trees, can be achieved by analyzing the 3D point cloud data using line detection (e.g., Hough transform) [17], intensity analysis [18], and advanced Deep Neural Networks (DNNs) (e.g., CA-PointNet++ [19], VEPL-Net [20], and RandLA-Net [21]). Despite its effectiveness, the broader use of airborne LiDAR

is limited by heavy payloads, high power consumption, and the need for high point density to map small objects [22]. For instance, high-voltage transmission lines are easier to map due to elevated positions, whereas lower voltage distribution lines are often obscured by dense forests, making detection more challenging [18].

### B. Opportunities in AD-Based Monitoring

As an alternative, ADs equipped with lightweight vision sensors offer a more cost-effective and practical solution. They can operate closer to the ground and capture high-resolution images in both the visible red, green, and blue (RGB) channels and infrared spectrums, providing detailed views of the environment [23]. This makes it particularly effective for monitoring both transmission and distribution lines. However, analyzing these captured images still relies on human observation, making it prone to errors and oversight.

Utility companies are beginning to pilot advanced wireless technologies, such as private Long Term Evolution (LTE) networks, to support intelligent sensors [24]. However, it is still challenging to manage the communication and control of many inspection ADs to support their transmission of a large volume of streaming image data. In addition, the critical control and non-payload data, including location and speed, demand robust communication that can be hindered by limitations in channel data rates. This can lead to data traffic congestion, potentially jeopardizing the safe navigation and operation of ADs, which in turn poses risks to power line infrastructure and public safety. Therefore, there is a critical need to develop automatic and real-time detection methods to enhance the efficiency and applicability of ADinspections.

### C. Image-Based Detection of Power Lines

Image-based automatic detection of power lines is challenging due to complex backgrounds and weak features [25]. Prior works have mainly utilized traditional image processing methods, such as Hough or Radon transforms to detect line segments [26], [27]. These methods are often complemented with prior information or clustering algorithms to assemble the segments into complete power lines. Edge extraction algorithms, such as Canny, Line Segment Detector (LSD), and Edge Drawing Lines (EDLines) have also been studied for power line detection [28], [29]. However, the performance of these methods heavily depends on carefully calibrated threshold parameters and handcrafted rules, which often lack adaptability. Moreover, these techniques have limited robustness for distinguishing power lines from other linear structures in noisy aerial images.

Deep learning neural networks, especially CNNs, excel at recognizing and learning features for object detection in images using extensive parameters and deep layers. Their significant successes span various applications, from autonomous driving to medical imaging [30]. Recent studies have explored the application of CNNs, for instance, VGG-19 and ResNet-50 for detecting power lines in aerial images [31], [32]. However, these approaches only classify images containing power lines

rather than for detection and positioning. CNNs for object detection tasks mostly use Horizontal Bounding Boxes (HBBs). These boxes encompass a large space compared to the power lines with thin structures and varying orientations, thus cannot accurately position power lines [33]. Therefore, some efforts focus on segmentation solutions that can detect power lines at the pixel level [34], [35], [36]. These efforts involve using UNet [37], a U-shaped CNN architecture specialized in image segmentation and its variants based on different backbones, such as VGG-19 [38] or GhostNet [39]. However, pixel-level line segmentation is inherently complex, time-consuming, and thus not ideal for real-time application. The YOLO algorithm is a popular object detection model known for its speed and accuracy [40]. First introduced in 2016, YOLO has iterated rapidly, including advancements in feature extraction, data augmentation, and model optimization. YOLOv8 [41], introduced in 2023, brings enhancements to multiple tasks. Its Oriented Bounding Box (OBB) task has the potential to solve the power line detection challenge with its rotatable capability.

This paper proposes an automatic real-time power line detection framework based on ADImages. It can accurately detect power lines with tight borders, quantitatively evaluate nearby vegetation encroachment, and send location-based alerts when risks are detected. The main contributions are listed as follows.

- We introduce PowerLine-YOLOv8 (PL-YOLOv8), an enhanced version of the YOLOv8 algorithm, tailored for the specific challenges of power line detection. This model integrates a novel directional block composed of convolutional layers initialized with parameters and sizes derived from a directional filter bank. This bank uses specialized directional filters that are designed to detect the orientations and textures of power lines and their vicinity, enhancing the accuracy of OBBs for precise localization.
- PL-YOLOv8 represents the first adaptation of YOLOv8's OBB capabilities specifically for power line extraction, resolving the trade-off between real-time detection and precise, tight bounding. For training, we developed a dataset with segmented image tiles and custom OBB annotations, specifically designed for accurate power line detection tasks. This dataset is customized using the Transmission Tower and Power Line Aerial (TTPLA) image dataset, which features high-resolution ADimagery of power lines [42], [43].
- We also propose a post-processing algorithm that develops a vegetation encroachment metric to evaluate the proximity of vegetation to power lines in aerial images. This metric utilizes the OBB detection locations and image data such as RGB indices, texture analysis, and brightness measurements. It offers an effective alternative to the intensive task of employing deep-learning-based segmentation methods for tree detection.
- The proposed software framework is designed for deployment on ADonboard processors. It transmits Global Positioning System (GPS) locations and essential image data only when vegetation metrics exceed predefined thresholds or when real-time viewing is requested. This location-based alert system minimizes data transmission, reduces

TABLE I  
OVERVIEW OF DIFFERENT DATA RESOURCES AND TECHNIQUES

Data Resource	Main Technique	Power Line Detection	Vegetation Detection	Data Resolution	Computational Cost	Position Accuracy	Communication Load
Satellite SAR/ Optical Imagery	Stereo matching & NDVI [7]–[9]	No	Yes	Low	Medium	Low	High
	Adaboost, SVM [11], [12]	No	Yes	Medium	High	Medium	High
Airborne LiDAR (fixed-wing/ helicopter)	Hough Transform & Intensity analysis [16], [17]	Yes	No	Medium	Medium	Medium	High
	3D point cloud data classification with DNNs [18]–[20]	Yes	Yes	Medium	High	High	High
UAV-Based Cameras	Image processing (Canny, Hough Transform, etc.) [28], [29]	Yes	No	High	Low	Low	High
	CNN-based classification [31], [32]	Yes	No	High	Medium	Low	High
	UNet-based segmentation [33]–[35]	Yes	No	High	High	Medium	Medium
	<b>Proposed PL-YOLO</b>	<b>Yes</b>	<b>Yes</b>	<b>High</b>	<b>Medium</b>	<b>High</b>	<b>Low</b>

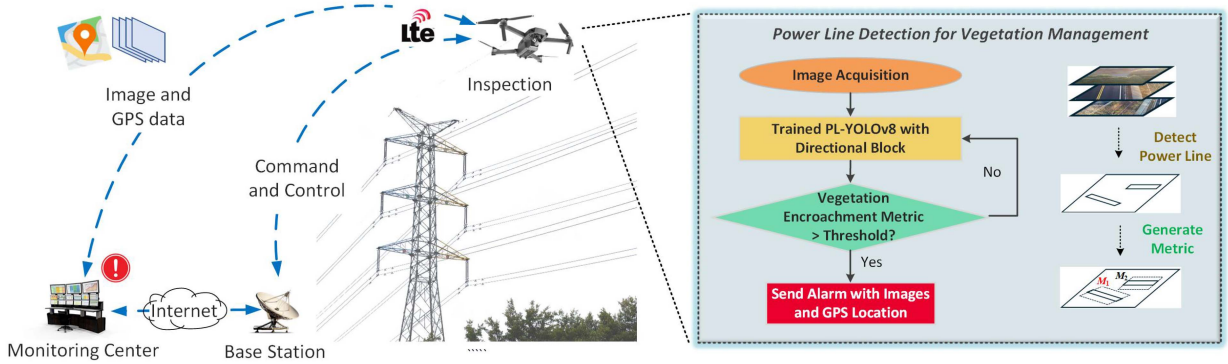


Fig. 1. Outline of PL-YOLO based power line detection for vegetation management.

wireless communication loads, and ensures high-quality image delivery. Its detailed, flexible views and low communication requirements make it ideal for monitoring both transmission and distribution lines.

The comparison of our proposed method with the existing literature is summarized in Table I. The rest of the paper is organized as follows. Section II outlines the workflow of the proposed framework. Section III discusses the PL-YOLOv8 network, including the innovative directional block. Section IV details the vegetation encroachment post-processing algorithm. Section V shows the experimental results. Section VI provides the study conclusions.

## II. OUTLINE OF PROPOSED FRAMEWORK

Our proposed framework introduces an end-to-end solution to manage power line inspections and vegetation encroachment, as shown in Fig. 1. Specifically, the software processes the image data as follows.

*Step 1:* The ADacquires images of the power lines while recording its GPS location. This data (images plus coordinates) is captured in real-time and can be stored locally on the AD's onboard processor.

*Step 2:* The onboard PLYOLOv8 algorithm analyzes these images to detect power lines, producing OBBs that accurately outline the detected lines. The PL-YOLOv8 is pretrained on the

proposed dataset or supplemented with additional datasets as needed.

*Step 3:* A vegetation encroachment metric module analyzes nearby pixels around the detected OBBs to evaluate how close or dense the vegetation is with respect to the power lines. It then computes an encroachment metric that quantifies potential risks.

*Step 4:* The system checks the metrics against predefined thresholds. If any metric exceeds the acceptable limit, an alarm event is triggered. Upon an alarm, the ADrelays the relevant images and corresponding GPS coordinates to the monitoring center via the base station. Operators can thus access the critical data in near real-time, determining whether immediate action is required.

By embedding the PLYOLOv8 and metric calculation modules directly on the AD, this workflow alleviates the communication load between the AD, base station, and monitoring center while preserving image quality. If real-time viewing is needed, the system can additionally stream selected frames or sensor data over the wireless link.

## III. ADVANCED PL-YOLOV8 FOR POWER LINE DETECTION

Previous object detection algorithms, such as the original Region-based CNN (R-CNN) and its successors (Fast R-CNN, Faster R-CNN), typically employ a two-stage process [44]. The localization stage employs a region proposal mechanism to pinpoint areas that potentially contain objects. This directs the

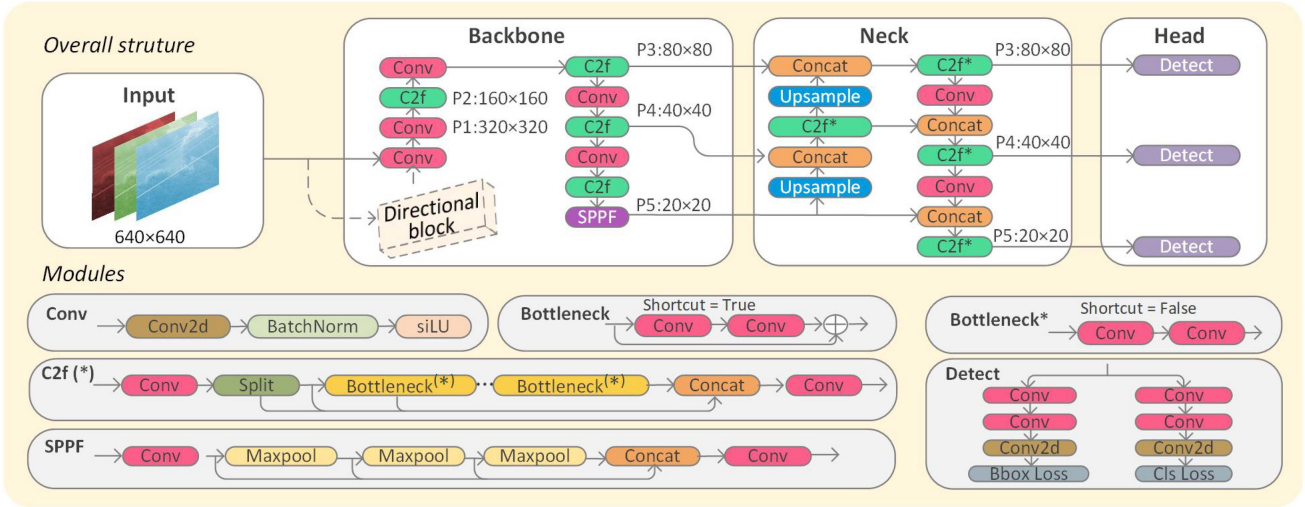


Fig. 2. Enhanced YOLO structure: PL-YOLOv8 with directional block.

subsequent neural network to concentrate on these areas, where it performs classification and regression tasks. This method achieves high accuracy through numerous regional proposals, but it also greatly limits time efficiency. YOLO revolutionizes real-time applications by employing an end-to-end neural network that simultaneously predicts bounding boxes and class probabilities. YOLOv8 builds on this by optimizing the architecture to improve object detection at various scales. It uses advanced convolutional layers and spatial pyramid pooling for better contextualization and spatial hierarchy preservation.

#### A. Overall Structure

Fig. 2 shows the PL-YOLOv8 network consisting of three main components: backbone, neck, and head. A directional block is incorporated at the beginning of the backbone, enhancing the standard YOLOv8. Further details on this block design are provided in Section III-C. The backbone extracts image features using Conv, SPPF (Spatial Pyramid Pooling-Fast), and C2f modules [45]. The Conv module includes a two-dimensional (2D) convolutional layer, batch normalization layer, and SiLU activation layer. SPPF can reduce computational load with three max-pooling layers that reduce the spatial dimensions of the feature maps. The C2f module enhances feature extraction using gradient diversion with Conv and residual modules (i.e., bottleneck). The neck employs a Feature Pyramid Network + Path Aggregation Network (FPN+PAN) structure to merge multi-scale features, enhancing detection accuracy for objects of varying sizes. The head uses a decoupled structure to optimize tasks of classification and detection separately, ensuring their respective optimal accuracy. In addition, the head adopts an anchor-free method by directly predicting bounding box coordinates from key points on the feature map. This eliminates the need for predefined anchor boxes in coupled heads, making the model more flexible and adaptive to various object sizes and shapes.

Given an example of a  $640 \times 640$  image, YOLOv8 down-samples and generates feature maps (P1–P5) at scales of  $320 \times 320$ ,  $160 \times 160$ ,  $80 \times 80$ ,  $40 \times 40$ , and  $20 \times 20$  pixels,

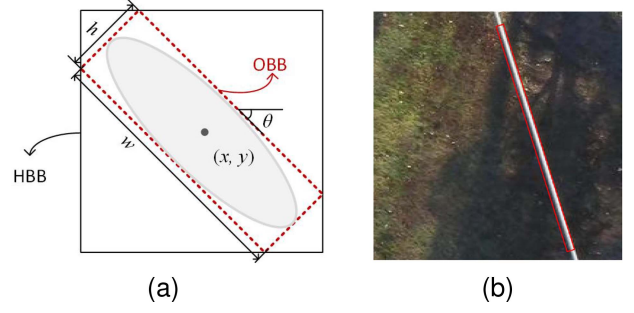


Fig. 3. OBB task: (a) OBB representation. (b) Power line detection example using the OBB concept.

respectively. P1 and P2 have larger and shallower feature maps and retain detailed spatial information crucial for detecting small objects. P4 and P5, with smaller and deeper feature maps, capture abstract features necessary for recognizing large objects. By integrating the P3, P4, and P5 layers, YOLOv8 leverages the strengths of multiple scales to detect objects of various sizes.

#### B. OBB Task Head

The OBB task improves traditional HBB detection by considering the object's orientation, which is particularly useful for power line detection, as shown in Fig. 3. An OBB is defined by its center coordinates  $(x, y)$ , width  $w$ , height  $h$ , and rotation angle  $\theta$ , allowing for tighter bounds and reducing background inclusion. The OBB localization loss is computed using the Probability-based Intersection over Union (ProbIoU) method [46] instead of the traditional IoU loss for HBBs. This method encodes the parameters  $(x, y, w, h, \theta)$  into a covariance matrix and calculates their various distance metrics, ensuring accurate localization loss by considering the object's position, size, and rotation.

#### C. Directional Block Design

The directional block is designed to comprise two convolutional layers, a leaky ReLU activation layer, and a channel

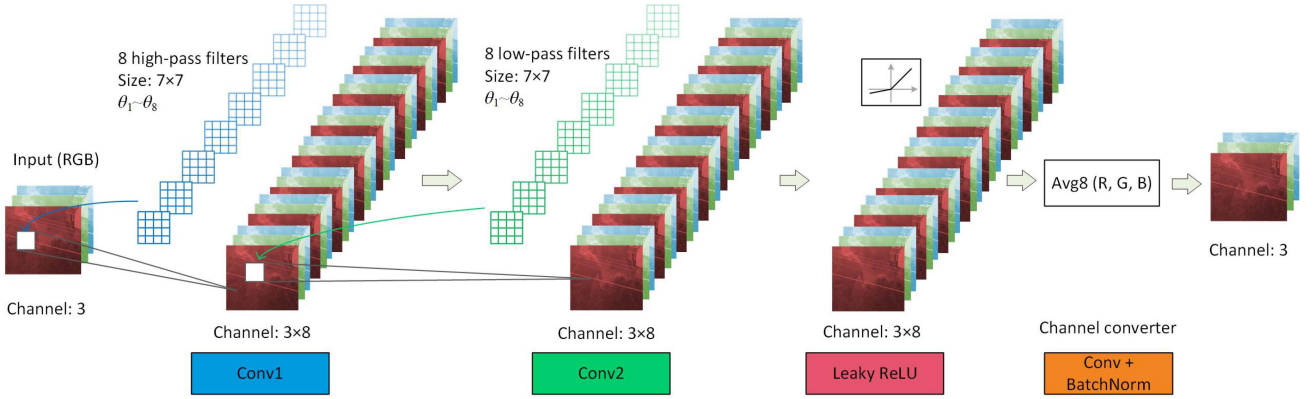


Fig. 4. Directional block containing 8 directional high-pass filters in its first stage.

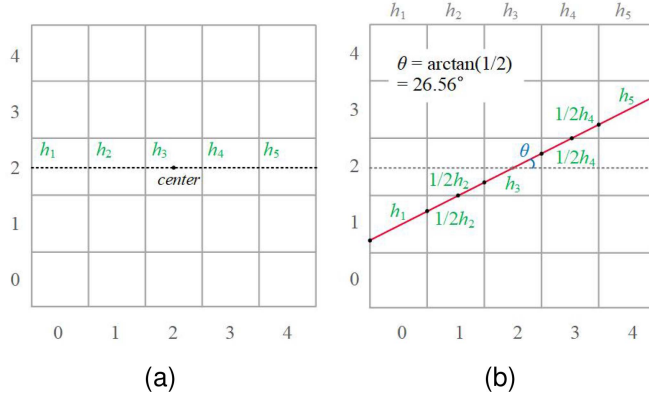


Fig. 5. 2D filter rotation example when  $n = 5$ . (a) Filter  $f_{\theta=0^\circ}(i, j)$ . (b) Filter  $f_{\theta=25.56^\circ}(i, j)$ .

converter, as illustrated in Fig. 4. The leaky ReLU activation helps mitigate negative values, preventing inactive neurons during training. The channel converter consists of a convolutional layer and a batch normalization layer. The convolutional layer features a  $1 \times 1$  kernel that averages directional features from 8 channels and converts them to 3 RGB channels. This configuration enables seamless integration into the YOLO backbone for further processing. The parameters in the convolutional layers are initialized using directional filters, as designed below. In image processing, it is customary to apply a low-pass filter to remove the noise while detecting the edges using an edge detection filter, which is essentially a high-pass filter. This approach generates a wavelet band-pass filter, as shown in (1).

$$h_{bp}[n] = (h_{lp} * h_{hp})[n] \quad (1)$$

Here,  $h_{bp}$  represents the band-pass filter. It is noted that the frequency response  $H_{bp}(e^{j\omega})$  of this filter is not identically zero across all frequencies  $\omega$  because the high- and low-pass filters are inherently not perfect. This results in a practical band-pass filter that does not entirely block all frequencies.

We rotate the one-dimensional (1D) prototype filter  $h_{bp}$  through eight directions within the range  $(\omega_1, \omega_2) \in (-\pi, \pi)$ , as described in the following paragraph and shown in Fig. 5. This yields a set of directional filters, with their smooth

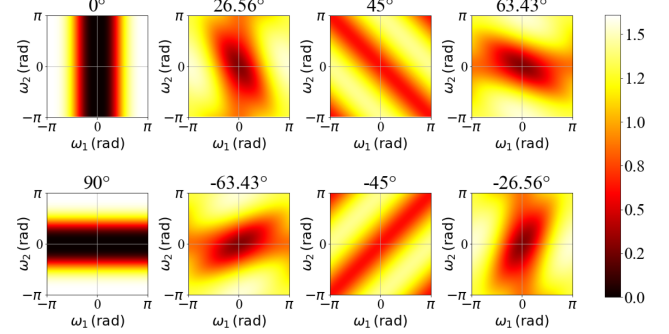


Fig. 6. 2D Frequency response plots,  $|H_{bp}(e^{j(\omega_1, \omega_2)})|$  for  $(\omega_1, \omega_2) \in (-\pi, \pi)$  at  $\theta = \{0^\circ, 26.56^\circ, 45^\circ, 63.44^\circ, 90^\circ, -63.44^\circ, -45^\circ, -26.56^\circ\}$ .

frequency responses shown in Fig. 6. These filters are designed to emphasize edges in all eight directions. This feature is vital for highlighting weak, straight-edge features of power lines against complex backgrounds, which is crucial for accurate detection and analysis. The designed filter parameters can initialize directional blocks in deep learning models to enhance directional feature extraction, allowing deeper layers in capturing structural details. This approach ensures that the network efficiently prioritizes essential image attributes from the start, improving the robustness of power line detection.

As pointed out above, the directional filters are created by rotating a 1D prototype filter with an impulse response of  $f_h = \{h_1, h_2, \dots, h_n\}$  into a 2D space across various angles parameterized by  $\theta$ . Illustrated in Fig. 5, we use a  $n \times n$  grid to represent the 2D filter  $f_\theta(i, j)$ , where  $i$  and  $j$  are the horizontal and vertical indices of the grid cells, respectively. A line at angle  $\theta$  crosses the grid's center with coordinates of  $(\frac{n}{2}, \frac{n}{2})$  and is defined by (2):

$$y = \left( x - \frac{n}{2} \right) \times \tan \theta + \frac{n}{2} \quad (2)$$

Specifically, the line segments in each grid denote the weights of the filter parameter. When  $\theta = 0$  and  $n$  is odd,  $f_0(i, \frac{n-1}{2})$  equals the original filter without rotation. Otherwise, the values in  $f_\theta(i, j)$  are in proportion to the line segment length  $L_\theta(i, j)$ , and are normalized by the line length in the center as  $L_\theta(\frac{n-1}{2}, \frac{n-1}{2})$ ,

**Algorithm 1:**  $L_\theta(i, j)$  Calculation.

---

**CALCULATE\_LINE\_LENGTHS** ( $n, \theta$ )

 $center \leftarrow n/2$ 
**for** each cell  $(i, j)$  in  $n \times n$  grid:

**determine** coordinates of four cell corners:

 $(\mathbf{X}_r, \mathbf{Y}_r)_{i,j} \leftarrow (i+r, j+r)$  **for**  $r = 0, 1$ 
**determine** intersection points on cell edges:

 $\mathbf{X}_{atY_r} \leftarrow (y - center)/\tan \theta + center$  **for**  $y \in \mathbf{Y}_r$ 
 $\mathbf{Y}_{atX_r} \leftarrow (x - center) \times \tan \theta + center$  **for**  $x \in \mathbf{X}_r$ 
**identify** two valid intersection points in the cell:

**if**  $X_0 < X_{atY_r} < X_1$  OR

 $Y_0 < Y_{atX_r} < Y_1$  **for**  $r = 0, 1$  is true:

 $\{(x_1, y_1), (x_2, y_2)\} \leftarrow \{(X_{atY_r}, Y_r), (X_r, Y_{atX_r})\}$ 
**Length:**  $L_\theta(i, j) \leftarrow \sqrt{(x_2 - x_1)^2 + (y_2 - y_1)^2}$ 
**return**  $L_\theta(i, j)$ 


---

as shown in (3).

$$f_\theta(i, j) = f_h(i) \times \frac{L_\theta(i, j)}{L_\theta(\frac{n-1}{2}, \frac{n-1}{2})} \quad (3)$$

where  $L_\theta(\frac{n-1}{2}, \frac{n-1}{2}) = \frac{1}{\cos \theta}$  when  $\theta \leq 45^\circ$ .  $L_\theta(i, j)$  is calculated by finding out the entry and exiting points in cell  $(i, j)$ , and calculating their Euclidean distances. The calculation algorithm is developed as follows.

For angles  $\theta \geq 45^\circ$ , the filter is generated by transposing  $f_{(90^\circ - \theta)}$ , which is calculated using the Algorithm 1. Within the directional block, the angles are set at  $\theta = \{0^\circ, \pm 26.56^\circ, \pm 45^\circ, \pm 63.44^\circ, 90^\circ\}$ . The initial parameters for the first two convolutional layers are created by rotating a high-pass filter and a low-pass filter, respectively. We selected the 1D high-pass prototype filter obtained from a seven-order half-band Lagrangian maximally flat low-pass filter with the following transfer function (4).

$$H_{hp}(z) = 1 + \frac{9}{16} ((-z)^1 + (-z)^{-1}) - \frac{1}{16} ((-z)^3 + (-z)^{-3}) \quad (4)$$

The high-pass filter is obtained using the transformation  $H_{hp}(z) = H_{lp}(-z)$ , and the corresponding impulse response of the high-pass filter is given by (5).

$$h_{hp}[n] = \left\{ \frac{1}{16}, 0, -\frac{9}{16}, 1, -\frac{9}{16}, 0, \frac{1}{16} \right\} \quad (5)$$

The low-pass filter used in the directional block is a wide-band low-pass filter, empirically designed. Its impulse response is shown in by (6).

$$h_{lp}[n] = \left\{ -\frac{1}{4}, -\frac{1}{2}, 1, 2, 1, -\frac{1}{2}, -\frac{1}{4} \right\} \quad (6)$$

The corresponding frequency responses within  $(-\pi, \pi)$  are shown in Fig. 7(a) and (b), respectively. Fig. 7(a) illustrates that the high frequencies are preserved while the low frequencies are suppressed, making the filter effective for edge detection. Fig. 7(c) illustrates that the low-pass filter, designed as a wide-band filter, suppresses high-frequency noise while preserving

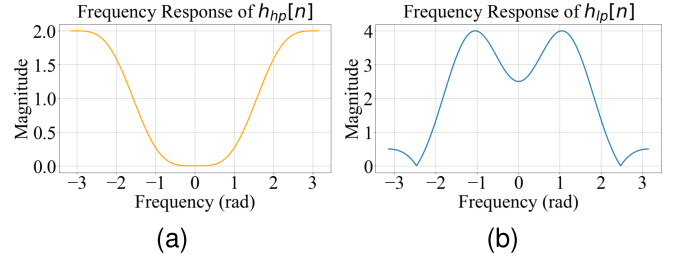


Fig. 7. Frequency responses of (a)  $h_{hp}[n]$  and (b)  $h_{lp}[n]$ , respectively.

low frequencies and maintaining essential structural details. Additionally, neither filter is ideal, allowing nonzero values within the suppressed frequency bands to ensure that critical information is retained.

The PL-YOLOv8 model with the initial directional block achieves a higher accuracy than standard PL-YOLOv8 in detecting power lines using OBBs.

#### IV. VEGETATION ENCROACHMENT METRIC DEVELOPMENT

Using the location results from power line detection with PL-YOLOv8, we devise a method to measure vegetation encroachment that assesses the density and growth of vegetation near power lines in the images. This approach combines a Greenness Index (GI) with a Tree-Grass Differentiation Index (TGDI) to create a comprehensive vegetation encroachment metric. Deep learning-based segmentation solutions are widely discussed and utilized for pixel-level vegetation detection [48]. However, they encounter significant computational challenges, especially for the detection of trees with diverse morphology. Our method employs RGB indices and image texture and brightness data, which can tackle the computational challenges associated with segmentation tasks in neural networks for tree detection.

##### A. Greenness Index

The GI is derived from the Green Red Vegetation Index (GRVI), which measures image greenness, complemented by a Gaussian filter that summarizes spatial information. GRVI is frequently utilized in image-based vegetation analysis and is represented in (7).

$$GRVI = \frac{G - R}{G + R} \quad (7)$$

where  $G$  and  $R$  are the green and red channel pixel values, respectively. This index effectively highlights vegetation by measuring the relative intensity of green compared to red light.

To aggregate the greenness information near power lines, we use a discrete, normalized Gaussian filter as outlined in (8).

$$G(g) = \frac{\exp\left(-0.5\left(\frac{g}{\sigma}\right)^2\right)}{\sum_g \exp\left(-0.5\left(\frac{g}{\sigma}\right)^2\right)} \quad (8)$$

Here,  $g$  represents the index, represented by the set  $\{-\frac{z-1}{2}, \dots, 0, \dots, \frac{z-1}{2}\}$ , where  $z$  is the filter size and  $\sigma$  is the standard deviation, influencing the filter's spread.

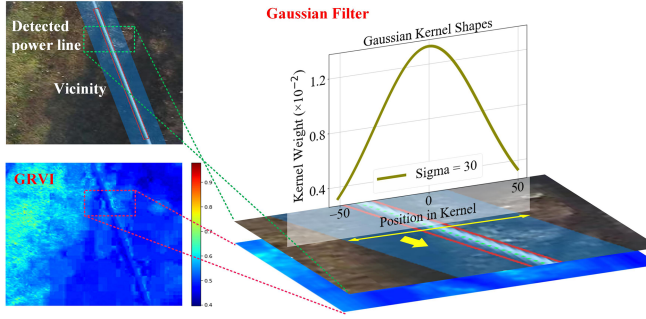


Fig. 8. Greenness index generation example.

Fig. 8 illustrates the application of the Gaussian filter near the power line. The power line's OBB is highlighted in red and defined by  $\{(u_c, v_c), (w, h), \theta\}$ . Here,  $(u_c, v_c)$  are the center coordinates,  $w$  and  $h$  the width and height, respectively, and  $\theta$  the rotation angle. The central line of the OBB is described by (9).

$$(u, v) = (u_c, v_c) + t \cdot (\cos \theta, \sin \theta) \quad (9)$$

where  $t$  varies from  $-\frac{w}{2}$  to  $\frac{w}{2}$ . Along this line,  $m$  evenly spaced pixels are sampled and defined in (10).

$$\begin{aligned} (u_k, v_k) &= \left( u_c + \left( -\frac{w}{2} + k \cdot \frac{w}{m} \right) \cos \theta, \right. \\ &\quad \left. v_c + \left( -\frac{w}{2} + k \cdot \frac{w}{m} \right) \sin \theta \right) \end{aligned} \quad (10)$$

where  $k$  ranges from 0 to  $m$ . The value of  $m$  is chosen as 100, considering the image size in our experiment is  $640 \times 640$ .

At each pixel sample  $(u_k, v_k)$ , the 1D Gaussian filter is centered and applied perpendicular to the central line. Let  $\mathbf{p}_\perp$  be the unit vector perpendicular to the line's direction at the point  $(x, y)$ . If the direction vector of the line is  $\mathbf{d} = (dx, dy)$ , then  $\mathbf{p}_\perp = (-dy, dx)$ . Points along the line perpendicular to  $\mathbf{d}$  at  $(u_k, v_k)$  are determined by (11).

$$(u_\perp, v_\perp)_g = (u_k, v_k) + g \cdot \mathbf{p}_\perp \quad (11)$$

Here,  $g$  represents the index in the Gaussian kernel, and  $\mathbf{p}_\perp$  is normalized for uniform spacing.

Next, the weighted greenness value  $W(k)$  for each position  $(u_k, v_k)$  along the power line is calculated as a weighted sum of the GRVI values using Gaussian weights, as shown in (12).

$$W(k) = \sum_{g=-\frac{n-1}{2}}^{\frac{n-1}{2}} I(u_\perp, v_\perp)_g \cdot G(g) \quad (12)$$

Here,  $I(u_\perp, v_\perp)_g$  denotes the GRVI value at each perpendicular pixel indexed by  $g$ , and  $G(g)$  is the corresponding Gaussian kernel weight. This results in a set of  $\mathbf{W}(k)$  values for the power line. Finally, a composite greenness index  $GI$  is derived by considering both the maximum and the average of these values, as shown in (13).

$$GI = \max(\mathbf{W}(k)) + \text{mean}(\mathbf{W}(k)) \quad (13)$$

The GI is specifically designed to provide a comprehensive evaluation of vegetation and its proximity to power lines. This index effectively captures both extreme and typical greenness scenarios near the power lines, facilitating a robust assessment of vegetation encroachment. Additionally, it employs a Gaussian filter to process spatial information, prioritizing areas closer to the power line with higher weights while assigning lower weights to farther regions. As a result, the GI provides a reliable measure for monitoring vegetation health and density around power lines.

### B. Vegetation Encroachment Metric

The GI provides color-based information from images, which can make it challenging to distinguish between highly green grasslands and trees. To address this issue, we incorporate the TGDI [49], which utilizes the visual distinctions between grasslands and tree crowns; grass typically appears brighter and smoother, while tree crowns are characterized by their darker and more textured appearance. The TGDI is defined as follows in (14).

$$TGDI = -\log_{10}(T) \times B \quad (14)$$

Here,  $T$  denotes the proportion of pixels identified as edges by the Canny algorithm, reflecting the image's texture.  $B$  represents the average grayscale values of the pixels, indicating the image's brightness. Since brightness is a more significant factor than texture in differentiating grasslands from tree crowns, the texture component  $T$  is adjusted by applying a logarithmic transformation, serving as an adjustment coefficient in the index. In this formulation, a higher TGDI value indicates the presence of grass, while a lower value suggests the presence of trees.

Combining this with the GI, we derive a final metric for vegetation encroachment, as represented in (15).

$$M = \alpha \cdot GI + \beta \cdot TGDI \quad (15)$$

Here,  $\alpha$  and  $\beta$  are coefficients that calibrate the contribution of each index to the overall metric, ensuring a balanced assessment of vegetation presence. Notably,  $\beta$  is set to a negative value to ensure that a higher  $M$  indicates a higher likelihood of tree presence, aligning with the intended interpretation of the metric.

## V. EXPERIMENT RESULTS

The proposed framework was developed and demonstrated using Python 3.10, leveraging its library support for deep learning and computer vision applications. Model design and implementation were carried out using PyTorch, with Spyder as the development environment and Anaconda for environment management. The effectiveness of the proposed PL-YOLOv8 and vegetation encroachment metric is demonstrated using a comprehensive public power infrastructure dataset, TTPLA [42], [43]. This dataset comprises ADlow-altitude aerial images of transmission towers and power lines collected from two states in the U.S. We preprocessed the dataset into appropriate image sizes and generated corresponding OBB annotations. The dataset preprocessing, detection results, evaluation, and assessment are discussed as follows.



Fig. 9. OBB annotation generation in an original image.



Fig. 10. Image tiles containing OBB annotations.

#### A. Data Preprocessing

The TTPLA dataset consists of 1,242 images with a resolution of  $3,840 \times 2,160$  pixels and includes manually labeled 10,075 instances of power lines. It can be utilized for the detection and segmentation tasks. For our purposes, we used only the power line data. We developed an automatic labeling method that converts segmentation annotations to OBB annotations. The segmentation annotations are polygons formed by a set of points along the instance edges. We used the *convexHull* and *minAreaRect* functions in OpenCV to generate OBBs that enclose the polygons. Fig. 9 illustrates the original polygon annotations (in blue) and the newly generated OBB annotations (in red). These OBB annotations efficiently enclose the power line within the minimal rectangular area, showcasing their effectiveness.

Furthermore, we divided the original images into  $640 \times 640$  tiles/sub-images. This ensures that the power lines in images are processed thoroughly, preserving important details without substantial loss during resizing. The OBB annotations were generated for each tile by adjusting and aligning with the boundaries. Fig. 10 highlights tiles containing power lines, which are preserved in the curated dataset. This dataset, named TTPLA-Tile-OBB, now comprises 17,178 images of size  $640 \times 640$  pixels, with accurate OBB annotations for power lines. It was then divided into training, validation, and test sets with an 8:1:1 ratio.

#### B. Power Line Detection Results

We conducted various training scenarios using different datasets and models to evaluate performance. The original and preprocessed TTPLA dataset are used to train both the standard YOLOv8 model and the proposed PL-YOLOv8 across four different model sizes: nano ( $n$ ), small ( $s$ ), medium ( $m$ ), and large ( $l$ ), respectively. They are scaled by the depth and width factors ( $d$  and  $w$ ), which determine the number of layers (depth) and the number of channels per layer (width) in the network, thereby resulting in different numbers of parameters, as shown in Table III.

The models are compared with the Yolact++ models with backbones of ResNet50 and ResNet101 [50]. Yolact++ is an upgraded variation of Yolact, a member of the YOLO family that enhances the YOLO architecture by adding a mask branch to perform instance segmentation tasks. The training cases and evaluation results are presented in Table II. Their detection results of power lines are showcased in Fig. 11. The performance metrics used across the models include  $AP^{50}$  and  $AP^{50-95}$ . The  $AP^{50}$  represents average precision at an IoU (intersection over union) threshold of 50%, while  $AP^{50-95}$  computes the average precision at IoU thresholds ranging from 50% to 95%, in 5% increments.

The Yolact++ model can detect both traditional HBB and masks, providing a baseline for ADaerial image-based power line detection [43], [50]. While masks allow pixel-level detection of power lines, their accuracy is relatively low, as shown in Table II. The quality of masks is not high with discontinuous pixels and missing detections, as shown in Fig. 11(a). Comparatively, the HBB tasks have a relatively higher accuracy, achieving an  $AP^{50}$  of 42.32% by Yolact++ (ResNet101). However, it fails to frame power lines with constrained bounds.

OBB tasks were anticipated to resolve the limitations observed in mask and HBB tasks. When employing the modified dataset (TTPLA-Tile-OBB) which comprises tiles to train the model, there is a significant improvement in accuracy across all sizes of YOLOv8 ( $n, s, m, l$ ). The  $AP^{50}$  increases to 69.00%, 76.33%, 70.70%, and 73.22%, respectively. Fig. 11(b) shows that the YOLOv8 model, using YOLOv8( $l$ ) as an example, effectively detects power lines with OBBs. However, a missing detection is evident in the second image of Fig. 11(b) when compared to Fig. 11(c). The proposed advanced PL-YOLOv8( $n$ ) model improves  $AP^{50}$  by 9.24% and  $AP^{50-95}$  by 7.48%, while PL-YOLOv8( $s, m, l$ ) models improve  $AP^{50}$  and  $AP^{50-95}$  by 1% to 2%. Fig. 11(c) illustrates the enhanced detection capabilities of these models, as shown by the results using PL-YOLOv8( $l$ ). These models generally achieve higher confidence scores compared to the standard YOLOv8 and excel at detecting power lines with weak features.

Additionally, we investigated the impact of directional block enhancement on PL-YOLOv8( $s$ ) using different training modes. Table IV presents the results. While freezing the directional filter layers ensures consistent directional feature extraction for the deep layers, it results in performance similar to the original YOLO models due to less flexibility. In the mixed training mode, the directional layers are frozen for the initial 1800 epochs and

TABLE II  
COMPARISON OF OBJECT DETECTION MODELS

Model	Image Size	Dataset	Task	AP <sup>50</sup>	AP <sup>50–90</sup>	FPS
Yolact++ (ResNet50)	700 × 700	Original TTPLA	Mask	5.11%	1.64%	9.04
Yolact++ (ResNet101)			HBB	41.45%	22.29%	
YOLOv8(n)	640 × 640	TTPLA-Tile-OBB	Mask	5.38%	1.92%	9.72
<b>PL-YOLOv8(n)</b>			HBB	42.32%	22.37%	
YOLOv8(s)			OBB	69.00%	36.02%	345
<b>PL-YOLOv8(s)</b>				<b>78.24%</b>	<b>43.50%</b>	<b>97</b>
YOLOv8(m)				76.33%	41.14%	151.51
<b>PL-YOLOv8(m)</b>				<b>78.14%</b>	<b>44.32%</b>	<b>49.50</b>
YOLOv8(l)				70.70%	40.50%	60.24
<b>PL-YOLOv8(l)</b>				<b>71.94%</b>	<b>41.14%</b>	<b>20.37</b>
YOLOv8(l)				73.22%	41.39%	35.08
<b>PL-YOLOv8(l)</b>				<b>74.60%</b>	<b>43.38%</b>	<b>16.47</b>

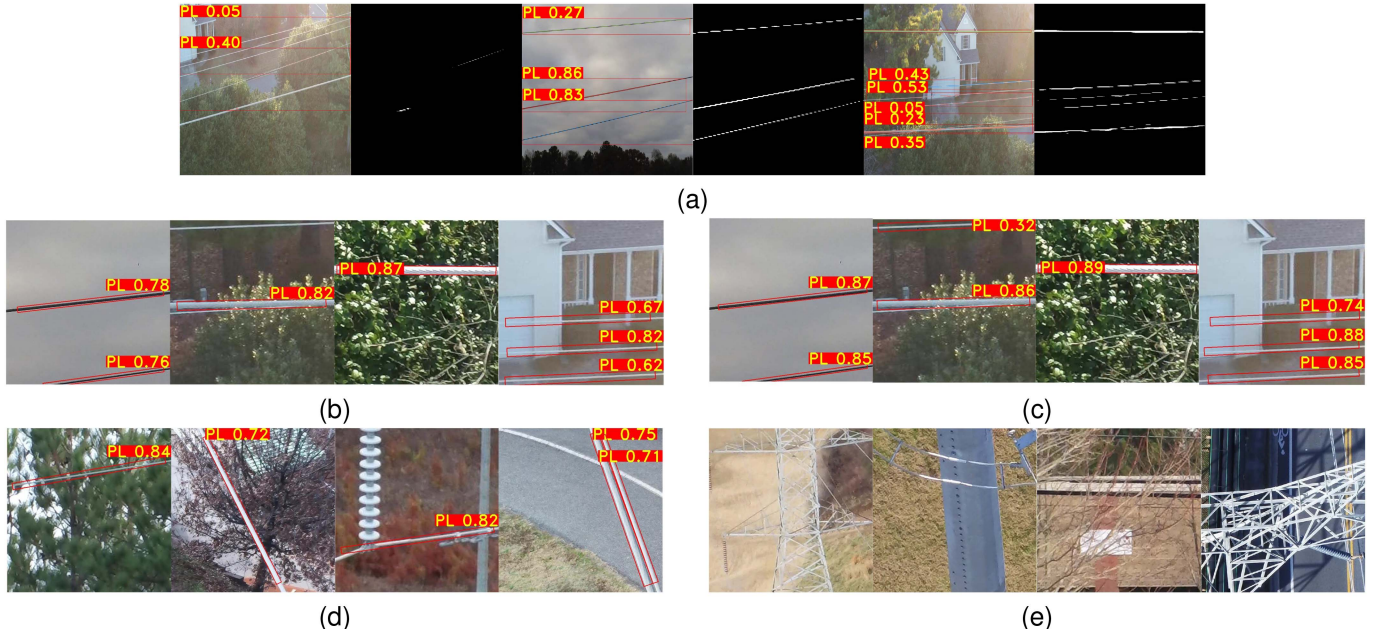


Fig. 11. Examples of detection results using various models and datasets. (a) HBB and mask detection with the Yolact++(ResNet101) model on TTPLA dataset. (b) OBB detection with YOLOv8(l) model on TTPLA-Tile-OBB dataset. (c) OBB detection with PL-YOLOv8(l) model on TTPLA-Tile-OBB dataset. (d) Exceptional OBB detection with PL-YOLOv8(l) model. (e) Power lines that are not detected by either YOLOv8(l) or PL-YOLOv8(l) models.

TABLE III  
YOLOv8 OBB MODEL SIZES

Model Size	Depth Factor $d$	Width Factor $w$	Params (M)
$n$	0.33	0.25	3.1
$s$	0.33	0.50	11.4
$m$	0.67	0.75	26.4
$l$	1	1	44.5

TABLE IV  
COMPARISON OF DIFFERENT TRAINING MODE FOR DIRECTIONAL BLOCK

Models	Directional block	AP <sup>50</sup>	AP <sup>50–95</sup>
PL-YOLOv8(s)	Frozen	76.30%	40.83%
PL-YOLOv8(s)	Trainable	78.14%	44.32%
PL-YOLOv8(s)	Mixed	77.26%	43.67%

trained for the final 200 epochs. This strategy enables the network to stabilize feature extraction in the early stages, allowing it to later adapt to more complex patterns to enhance model performance. PL-YOLOv8(s) in the mixed training mode has a

0.96% improvement in  $AP^{50}$  and a 2.84% increase in  $AP^{50–95}$  compared to the frozen mode. Making the directional filter layers fully trainable provides greater adaptability, enabling the initial layers to extract meaningful directional features from the start and resulting in the best performance gains.

Fig. 11(d) showcases additional power lines that were not detected by YOLOv8(l). These lines exhibit either non-typical features like those connected to insulators or weak features against a complex or confusing background. The superior performance of the enhanced PL-YOLOv8 models is attributed to directional filters that excel in extracting features from various orientations and complicated textures. Fig. 12 visually displays the binarized textures extracted by these directional filters at 0°, 45°, and 90°, showcasing their effectiveness in feature detection. Fig. 11(e) illustrates power line cases that were not detected by either the YOLOv8(l) or PL-YOLOv8(l) models. These cases have weak line characteristics that are either too distant to be detected or are obscured by complex transmission tower structures or tree branches, making detection challenging.

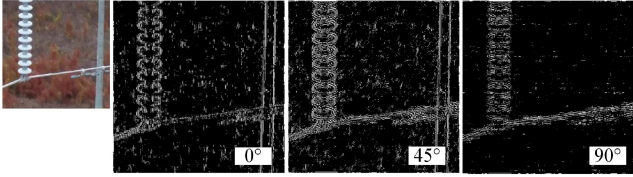


Fig. 12. Edge enhancement with directional filtering at angles  $0^\circ$ ,  $45^\circ$ ,  $90^\circ$ .

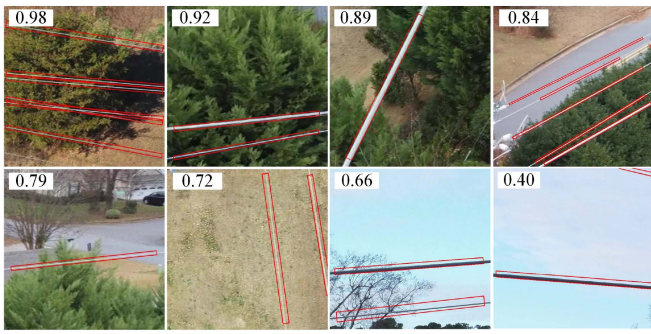


Fig. 13. Vegetation encroachment metrics: sorted image examples.

### C. Real-Time Detection Capability Evaluation

The real-time detection capability of the proposed models was evaluated by testing their frame rates on an NVIDIA GeForce RTX 4060 Laptop GPU (8188 MiB), as shown in Table II. While PL-YOLOv8 models generally produce lower FPS than standard YOLOv8, the PL-YOLOv8(n) model maintains a high performance of 97 FPS, which far exceeds the typical real-time threshold of 15–30 FPS. While ADprocessors (e.g., Jetson modules) have stricter power and thermal constraints, this performance margin allows effective down-scaling. Further optimizations, such as TensorRT deployment, can enhance FPS performance on embedded platforms (e.g., Nvidia Jetson Xavier NX). This evaluation demonstrates the proposed model’s capability for accurate and real-time power line detection, showing its potential for ADfield applications.

### D. Evaluation of Vegetation Encroachment Metric Method

The vegetation encroachment metric method was evaluated using 1,000 images from the test dataset. Vegetation encroachment metrics were calculated for each image by evaluating the proximity of vegetation to power lines, using power line detections from PL-YOLOv8. Examples of vegetation encroachment metrics are shown in Fig. 13, demonstrating how these values can indicate trends in vegetation encroachment. For evaluation, the continuous metric was converted into a binary classification problem using a threshold. If the metric value was greater than or equal to the threshold, the image was classified as alarming for vegetation encroachment; otherwise, it was not. The ground truth for the images was generated by manually labeling them into two classes: alarm and non-alarm. Based on the ground truth and prediction results, the performance was then evaluated using metrics such as accuracy, precision, recall, and F1 score.

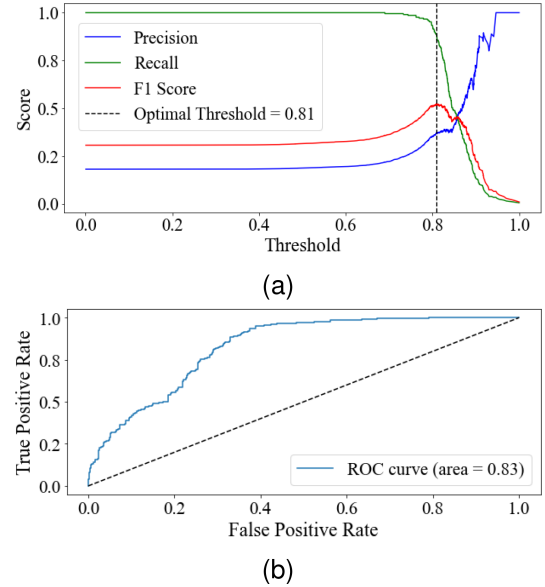


Fig. 14. Evaluation of the vegetation metric method: (a) Precision, recall, and F1 scores over different thresholds. (b) ROC curve and AUC.

TABLE V  
EVALUATION METRICS AT OPTIMAL THRESHOLD

Optimal Threshold	Accuracy	Precision	Recall	F1 Score
0.81	0.71	0.37	0.89	0.52

Precision is the ratio of true positives to the total positive detections (both true positives and false positives), reflecting the model’s accuracy in identifying actual alarms. Recall, or sensitivity, is the ratio of true positives to all actual positives (true positives and false negatives), showing the model’s ability to identify all potential hazards. The F1 score reflects the balance between precision and recall, showing the model’s effectiveness in accurately identifying trees at risk of vegetation encroachment while maintaining high sensitivity and precision to minimize false alarms.

To find the optimal threshold, we plotted the precision, recall, and F1 scores as shown in Fig. 14(a). The optimal threshold was determined to be 0.81, where the F1 score is highest. The evaluation metrics at this threshold are presented in Table V. With this threshold, the higher recall is prioritized over precision, aligning with the goal that false negatives are more critical than false positives in vegetation management since false negatives (missed encroachments) could result in severe consequences such as power outages, fires, or safety hazards. This ensures that most encroachment cases are identified, reducing the risk of missing high-priority areas requiring immediate attention. Fig. 14(b) illustrates the Receiver Operating Characteristic (ROC) curve, which displays the performance of the classification model across all thresholds. This curve plots the true positive rate against the false positive rate. The Area Under ROC Curve (AUC) indicates the model’s ability to distinguish between positive (alarm) and negative (non-alarm) classes across different thresholds. An AUC of 0.83 demonstrates the model’s high discrimination capability, effectively distinguishing between images with and without alarms. This

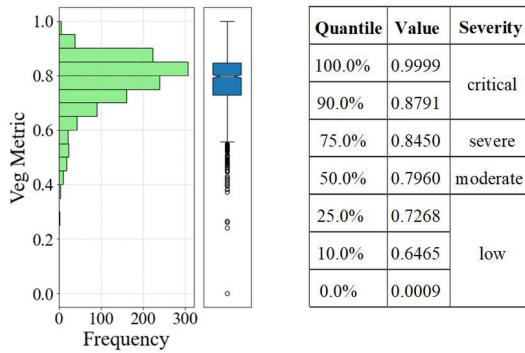


Fig. 15. Severity levels based on metric percentiles.

result demonstrates the effectiveness of the proposed vegetation encroachment metric in effectively identifying potential risks.

The evaluation demonstrates that the proposed metric effectively captures the severity of vegetation encroachment. Therefore, in addition to relying on a hard predefined threshold, we also propose a level-based method to indicate severity and prioritize risk areas. Fig. 15 illustrates the distribution of the metric data and provides an example of the severity table, which is based on the metric percentiles:

- *Critical*: greater than the 90th percentile ( $> 0.8791$ ).
- *Severe*: between the 75th and 90th percentiles ( $0.8450 - 0.8791$ ).
- *Moderate*: between the 50th and 75th percentiles ( $0.7961 - 0.8450$ ).
- *Low*: below the 50th percentile ( $< 0.7961$ ).

This approach avoids using a hard threshold and is particularly useful for datasets lacking ground truth for vegetation encroachment. It can provide utilities with severity levels to prioritize maintenance schedules, optimize resource allocation, and identify high-risk areas for proactive intervention.

## VI. CONCLUSION

We proposed an advanced YOLO-based deep learning framework for effectively detecting power lines and evaluating vegetation encroachment using Aerial images. The framework offers a PL-YOLOv8 neural network, which enhances the traditional YOLOv8 with an innovative directional block for efficiently extracting weak features of thin and long power lines and their vicinity in complex backgrounds. Additionally, it is the first to use OBBs to detect power lines, providing precise localization with high accuracy. The comparative analysis indicates that the proposed PL-YOLOv8(n) model achieves an  $AP^{50}$  of 78.24%, and a frame rate of 97 FPS.

In addition, a vegetation encroachment metric method is introduced to assess the proximity of nearby vegetation to power lines based on the OBB location. This approach offers a straightforward and effective alternative to complex segmentation tasks for tree detection by leveraging image RGB indices, textures, and brightness to assess vegetation encroachment. The results demonstrate promising effectiveness, with an accuracy of 0.71 and an F1 score of 0.52 in our dataset.

## REFERENCES

- [1] S. Moon, “California’s second-largest wildfire was sparked when power lines came in contact with a tree, Cal fire says,” *CNN*, Jan. 2022. Accessed: Jun. 18, 2025. [Online]. Available: <https://edition.cnn.com/2022/01/05/us/dixie-fire-power-lines-cause-pge>
- [2] M. Biesecker, “Takeaways from AP report on Maui fire investigation,” *US News*, Sep. 2023. Accessed: Jun. 18, 2025. [Online]. Available: <https://apnews.com/article/wildfires-maui-hawaii-electricityutility-investigation-76962306e8e2d0867c79de8490d58a5d>
- [3] B. Potter, “How to save America’s transmission system,” *Inst. Prog.*, Feb. 2024.
- [4] L. Matikainen et al., “Remote sensing methods for power line corridor surveys,” *ISPRS J. Photogrammetry Remote Sens.*, vol. 119, pp. 10–31, 2016.
- [5] L. Yan, H. Ailing, L. Sha, L. Xingkai, W. Wenhao, and L. Tao, “High voltage power line scattering feature analysis in multi SAR sensors and dual polarization,” in *Proc. 2nd Int. Workshop Earth Observation Remote Sens. Appl.*, Shanghai, China, 2012, pp. 225–229.
- [6] F. M. E. Haroun, S. N. M. Deros, and N. Md Din, “A review of vegetation encroachment detection in power transmission lines using optical sensing satellite imagery,” 2020, *arXiv:2010.01757*.
- [7] J. Ahmad, A. S. Malik, and L. Xia, “Vegetation monitoring for high-voltage transmission line corridors using satellite stereo images,” in *Proc. Nat. Postgraduate Conf.*, Perak, Malaysia, 2011, pp. 1–5.
- [8] Y. Kobayashi, G. G. Karady, G. T. Heydt, and R. G. Olsen, “The utilization of satellite images to identify trees endangering transmission lines,” *IEEE Trans. Power Del.*, vol. 24, no. 3, pp. 1703–1709, Jul. 2009.
- [9] C. Xiao, R. Qin, X. Huang, and J. Li, “Individual tree detection from multi-view satellite images,” in *Proc. IGARSS IEEE Int. Geosci. Remote Sens. Symp.*, 2018, pp. 3967–3970.
- [10] G. Goldbergs, S. Maier, S. Levick, and A. Edwards, “Limitations of high resolution satellite stereo imagery for estimating canopy height in australian tropical savannas,” *Int. J. Appl. Earth Observation Geoinformation*, vol. 75, pp. 83–95, 2019.
- [11] M. Gazzea, M. Pacevicius, D. O. Dammann, A. Sapronova, T. M. Lunde, and R. Arghandeh, “Automated power lines vegetation monitoring using high-resolution satellite imagery,” *IEEE Trans. Power Del.*, vol. 37, no. 1, pp. 308–316, Feb. 2022.
- [12] F. M. E. Haroun, S. N. M. Deros, M. Z. Bin Baharuddin, and N. Md Din, “Detection of vegetation encroachment in power transmission line corridor from satellite imagery using support vector machine: A features analysis approach,” *Energies*, vol. 14, no. 12, 2021, Art. no. 3393.
- [13] S. Rong, L. He, L. Du, Z. Li, and S. Yu, “Intelligent detection of vegetation encroachment of power lines with advanced stereovision,” *IEEE Trans. Power Del.*, vol. 36, no. 6, pp. 3477–3485, Dec. 2021.
- [14] Y. Liu, J. Shi, Z. Liu, J. Huang, and T. Zhou, “Two-layer routing for high-voltage powerline inspection by cooperated ground vehicle and drone,” *Energies*, vol. 12, no. 7, 2019, Art. no. 1385.
- [15] “2023 to 2025 electrical corporation wildfire mitigation plans,” Docket No. 2023-2025-WMPs, Pacific Gas and Electric Company (PG&E), Jan. 2024. Accessed: Jun. 18, 2025. [Online]. Available: [https://www.lspgridcalifornia.com/wpcontent/uploads/2024/12/2024-9-17\\_LSPGC\\_2023\\_WMP\\_R2\\_Clean.pdf](https://www.lspgridcalifornia.com/wpcontent/uploads/2024/12/2024-9-17_LSPGC_2023_WMP_R2_Clean.pdf)
- [16] J. Gardner, “Duke’s transmission vegetation management transformation,” *TD World*, Jun. 2023. Accessed: Jun. 18, 2025. [Online]. Available: <https://www.tdworld.com/vegetationmanagement/article/21265498/dukes-transmission-vegetation-managementtransformation>
- [17] Y. Liu, Z. Li, R. Hayward, R. Walker, and H. Jin, “Classification of airborne LIDAR intensity data using statistical analysis and hough transform with application to power line corridors,” in *Proc. Digit. Image Comput., Techn. Appl.*, Melbourne, VIC, Australia, 2009, pp. 462–467.
- [18] L. Zhu and J. Hyypää, “Fully-automated power line extraction from airborne laser scanning point clouds in forest areas,” *Remote Sens.*, vol. 6, no. 11, pp. 11267–11282, 2014.
- [19] G. Wang, L. Wang, S. Wu, S. Zu, and B. Song, “Semantic segmentation of transmission corridor 3D point clouds based on CA-PointNet,” *Electronics*, vol. 12, no. 13, 2023, Art. no. 2829.
- [20] M. Cano-Solis, J. R. Ballesteros, and G. SanchezTorres, “VEPL-Net: A deep learning ensemble for automatic segmentation of vegetation encroachment in power line corridors using UAV imagery,” *ISPRS Int. J. Geo-Inf.*, vol. 12, no. 11, 2023, Art. no. 454.
- [21] F. Bahreini, A. Hammad, and M. Nik-Bakht, “Point cloud-based computer vision framework for detecting proximity of trees to power distribution lines,” in *Proc. Int. Symp. Automat. Robot. Construction*, 2024, pp. 730–737.

- [22] P. Hamelin et al., "Discrete-time control of LineDrone: An assisted tracking and landing UAV for live power line inspection and maintenance," in *Proc. Int. Conf. Unmanned Aircr. Syst.*, 2019, pp. 292–298.
- [23] N. Iversen, O. B. Schofield, L. Cousin, N. Ayoub, G. vom Bögel, and E. Ebeid, "Design, integration and implementation of an intelligent and self-recharging drone system for autonomous power line inspection," in *Proc. IEEE/RSJ Int. Conf. Intell. Robots Syst.*, 2021, pp. 4168–4175.
- [24] "Private 5G/4G networks a 2 billion opportunity in the utilities industry," *TD World*, Nov. 2023. Accessed: Jun. 18, 2025. [Online]. Available: <https://www.tdworld.com/smart-utility/article/21276776/private-5g-4g-networks-a-2-billion-opportunity-in-the-utilities-industry>
- [25] L. Yang, J. Fan, Y. Liu, E. Li, J. Peng, and Z. Liang, "A review on state-of-the-art power line inspection techniques," *IEEE Trans. Instrum. Meas.*, vol. 69, no. 12, pp. 9350–9365, Dec. 2020.
- [26] L. Baker, S. Mills, T. Langlotz, and C. Rathbone, "Power line detection using Hough transform and line tracing techniques," in *Proc. Int. Conf. Image Vis. Comput. New Zealand*, Palmerston North, New Zealand, 2016, pp. 1–6.
- [27] Y. Chen, Y. Li, and H. Zhang, "Automatic power line extraction from high resolution remote sensing imagery based on an improved radon transform," *Pattern Recognit.*, vol. 49, pp. 174–186, 2016.
- [28] M. Gerke and P. Seibold, "Visual inspection of power lines by U.A.S.," in *Proc. Int. Conf. Expo. Elect. Power Eng.*, 2014, pp. 1077–1082.
- [29] Ö. E. Yetgin, Z. Şentürk, and Ö. N. Gerek, "A comparison of line detection methods for power line avoidance in aircrafts," in *Proc. 9th Int. Conf. Elect. Electron. Eng.*, 2015, pp. 241–245.
- [30] A. Zhang et al., *Dive Into Deep Learning*. Cambridge, U.K.: Cambridge Univ. Press, 2023.
- [31] Ö. E. Yetgin, B. Benligiray, and Ö. N. Gerek, "Power line recognition from aerial images with deep learning," *IEEE Trans. Aerosp. Electron. Syst.*, vol. 55, no. 5, pp. 2241–2252, Oct. 2019.
- [32] H. Aboalia, S. Hussein, and A. Mahmoud, "Enhancing power lines detection using deep learning and feature-level fusion of infrared and visible light images," *Arabian J. Sci. Eng.*, vol. 50, pp. 987–999, 2024, doi: [10.1007/s13369-024-09043-0](https://doi.org/10.1007/s13369-024-09043-0).
- [33] P. Sharma, S. Saurav, and S. Singh, "Object detection in power line infrastructure: A review of the challenges and solutions," *Eng. Appl. Artif. Intell.*, vol. 130, 2024, Art. no. 107781.
- [34] M. He, L. Qin, X. Deng, S. Zhou, H. Liu, and K. Liu, "Transmission line segmentation solutions for UAV aerial photography based on improved UNet," *Drones*, vol. 7, 2023, Art. no. 274.
- [35] C. Xu, Q. Li, Q. Zhou, S. Zhang, D. Yu, and Y. Ma, "Power line-guided automatic electric transmission line inspection system," *IEEE Trans. Instrum. Meas.*, vol. 71, 2022, Art. no. 3512118.
- [36] G. Han, M. Zhang, Q. Li, X. Liu, T. Li, and L. Zhao, "A lightweight aerial power line segmentation algorithm based on attention mechanism," *Machines*, vol. 10, 2022, Art. no. 881.
- [37] O. Ronneberger, P. Fischer, and T. Brox, "U-Net: Convolutional networks for biomedical image segmentation," in *Proc. 18th Int. Conf. Med. Image Comput. Comput.-Assist. Intervention*, Munich, Germany, 2015, pp. 234–241.
- [38] K. Simonyan and A. Zisserman, "Very deep convolutional networks for large-scale image recognition," 2014, *arXiv:1409.1556*.
- [39] K. Han, Y. Wang, Q. Tian, J. Guo, C. Xu, and C. Xu, "GhostNet: More features from cheap operations," in *Proc. IEEE/CVF Conf. Comput. Vis. Pattern Recognit.*, 2020, pp. 1580–1589.
- [40] J. Redmon, S. Divvala, R. Girshick, and A. Farhadi, "You only look once: Unified, real-time object detection," in *Proc. IEEE Conf. Comput. Vis. Pattern Recognit.*, 2016, pp. 779–788.
- [41] G. Jocher, A. Chaurasia, and J. Qiu, "Ultraalytics YOLO (Version 8.0.0) [Computer software]," 2023. [Online]. Available: <https://github.com/ultralytics/ultralytics>
- [42] B. Ruszczak, P. Michalski, and M. Tomaszewski, "Overview of image datasets for deep learning applications in diagnostics of power infrastructure," *Sensors*, vol. 23, no. 16, Aug. 2023, Art. no. 7171.
- [43] R. Abdelfattah, X. Wang, and S. Wang, "TTPLA: An aerial-image dataset for detection and segmentation of transmission towers and power lines," in *Proc. Asian Conf. Comput. Vis.*, 2020, doi: [10.1007/978-3-030-63486-5\\_29](https://doi.org/10.1007/978-3-030-63486-5_29). Accessed: Jun. 18, 2025. [Online]. Available: [https://openaccess.thecvf.com/content/ACCV2020/papers/Abdelfattah\\_TTPLA\\_An\\_Aerial-Image\\_Dataset\\_for\\_Detection\\_and\\_Segmentation\\_of\\_Transmission\\_ACCV\\_2020\\_paper.pdf](https://openaccess.thecvf.com/content/ACCV2020/papers/Abdelfattah_TTPLA_An_Aerial-Image_Dataset_for_Detection_and_Segmentation_of_Transmission_ACCV_2020_paper.pdf)
- [44] F. Feng, Y. Hu, W. Li, and F. Yang, "Improved YOLOv8 algorithms for small object detection in aerial imagery," *J. King Saud Univ. - Comput. Inf. Sci.*, vol. 36, no. 6, 2024, Art. no. 102113.
- [45] S. Ren, K. He, R. Girshick, and J. Sun, "Faster R-CNN: Towards real-time object detection with region proposal networks," *IEEE Trans. Pattern Anal. Mach. Intell.*, vol. 39, no. 6, pp. 1137–1149, Jun. 2017.
- [46] J. Murruarraga-Llerena, L. N. Kirsten, L. F. Zeni, and C. R. Jung, "Probabilistic intersection-over-union for training and evaluation of oriented object detectors," *IEEE Trans. Image Process.*, vol. 33, pp. 671–681, 2024.
- [47] S. F. Atici, R. Ansari, V. Allareddy, O. Suhaym, A. E. Cetin, and M. H. Elnagar, "Fully automated determination of the cervical vertebrae maturation stages using deep learning with directional filters," *PLoS One*, vol. 17, no. 7, 2022, Art. no. e0269198.
- [48] B. Ayhan et al., "Vegetation detection using deep learning and conventional methods," *Remote Sens.*, vol. 12, no. 15, 2020, Art. no. 2502.
- [49] Y. Qian, W. Zhou, C. J. Nyctch, L. Han, and Z. Li, "A new index to differentiate tree and grass based on high resolution image and object-based methods," *Urban Forestry Urban Greening*, vol. 53, 2020, Art. no. 126661.
- [50] D. Bolya, C. Zhou, F. Xiao, and Y. J. Lee, "YOLACT++: Better real-time instance segmentation," *IEEE Trans. Pattern Anal. Mach. Intell.*, vol. 44, no. 2, pp. 1108–1121, Feb. 2022.

**Shuaiwang Rong** received the M.S. degree in electric engineering from the Shanghai University of Electric Power, Shanghai, China, in 2018. She is currently working toward the Ph.D. degree with the University of Illinois Chicago, Chicago, IL, USA. Her research interests include deep learning, image processing, renewable energy integration, and power system protection.

**Lina He** received the Ph.D. degree in electrical engineering from University College Dublin, Dublin, Ireland, in 2014. From 2014 to 2017, she was a Project Manager and Senior Consultant with Siemens, Germany and Siemens, USA. She is currently an Assistant Professor with the Department of Electrical and Computer Engineering, University of Illinois Chicago, Chicago, IL, USA. Her research interests include power system resilience, renewable energy integration, power system security and operation, and AI applications in power systems.

**Salih Furkan Atici** received the Ph.D. and M.S. degrees in electrical and computer engineering from the University of Illinois Chicago, Chicago, IL, USA, in 2020 and in 2024, respectively. He is currently with Apple Inc., Cupertino, CA, USA. His research interests include deep learning, image processing, video processing, video codec, and machine learning.

**Ahmet Enis Cetin** (Fellow, IEEE) received the B.Sc. degree from METU, Ankara, Türkiye, and the Ph.D. degree from the University of Pennsylvania, Philadelphia, PA, USA, in 1987. From 1987 to 1989, he was an Assistant Professor with the University of Toronto, Canada. From 1987 to 2017, he was a Faculty Member with Bilkent University. He was also a Visiting Professor with Bellcore in 1988, University of Minnesota from 1996 to 1997, and UC San Diego from 2016 to 2017. He is currently a Professor with the Department of Electrical and Computer Engineering, University of Illinois Chicago (UIC), Chicago, IL, USA. His research interests include theoretical and applied machine learning, signal, image, and video processing, biomedical signal processing, infrared and chemical sensor signal processing in cyber-physical systems (CPS). His group introduced the concept of adaptive prediction and split vector quantization for Line Spectral Frequency representation. This concept was used in ITU speech coding standards including G.729, G.723.1, and GSM EFR.

He became Fellow of IEEE for his contributions to signal and image recovery in 2010. He is the Editor-in-Chief of *Signal, Image and Video Processing*, Springer-Nature. He was the recipient of the best paper award for his camera-based wildfire detection work in a conference organized by UNESCO and Cyprus Presidency of the European Union. He is one of the Co-Founders of the multi-national smart wide angle OEM camera company Oncam-Grandeye, U.K. He was the CEO/CTO of Grandeye, Turkey between 2003-2013. Oncam-Grandeye cameras won design and innovation awards in IFSEC, U.K., ISC WEST, Las Vegas, and trade fairs.